Journal of Colloid and Interface Science 673 (2024) 60–69

Contents lists available at ScienceDirect

Journal of Colloid And Interface Science

journal homepage: www.elsevier.com/locate/jcis

Regular Article

Construction of coherent interface between Cu_2O and CeO_2 *via* electrochemical reconstruction for efficient carbon dioxide reduction to methane

Xiong Yan [a], Shuo Wang [d], Ziliang Chen [a,c], Yunjie Zhou [a], Hui Huang [a,*], Jie Wu [a], Tiwei He [a], Hongyuan Yang [b], Likai Yan [d,*], Kaili Bao [a], Prashanth W. Menezes [b,c,*], Zhenhui Kang [a,e,*]

[a] *Institute of Functional Nano & Soft Materials (FUNSOM), Jiangsu Key Laboratory for Carbon-Based Functional Materials & Devices, Soochow University, 199 Ren'ai Road, Suzhou 215123, Jiangsu, China*
[b] *Department of Chemistry: Metalorganics and Inorganic Materials, Technische Universität Berlin, Straße des 17 Juni 135, Sekr. C2, 10623 Berlin, Germany*
[c] *Material Chemistry Group for Thin Film Catalysis-CatLab, Helmholtz-Zentrum Berlin für Materialien und Energie, Albert-Einstein-Str. 15, 12489 Berlin, Germany*
[d] *Institute of Functional Material Chemistry, Key Laboratory of Polyoxometalate Science of Ministry of Education, Faculty of Chemistry, Northeast Normal University, Changchun 130024, China*
[e] *Macao Institute of Materials Science and Engineering (MIMSE), MUST-SUDA Joint Research Center for Advanced Functional Materials, Macau University of Science and Technology, Taipa 999078, Macao*

GRAPHICAL ABSTRACT

The *in-situ* electrochemically reconstructed Cu_2O/CeO_2 from CuO/CeO_2 has been demonstrated to be effective for electrocatalytic carbon dioxide reduction, delivering a high selectivity, activity, and stability for producing CH_4.

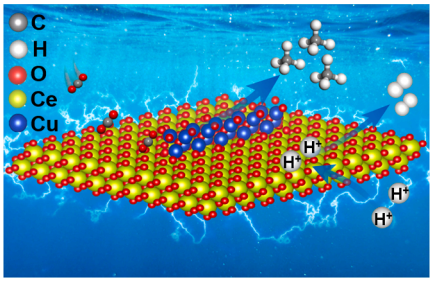

ARTICLE INFO

Keywords:
Metal oxide
Rare earth metal
Heterointerface
Activity and selectivity
Carbon dioxide reduction

ABSTRACT

Developing an efficient electrocatalyst that enables the efficient electrochemical conversion from CO_2 to CH_4 across a wide potential range remains a formidable challenge. Herein, we introduce a precatalyst strategy that realizes the *in situ* electrochemical reconstruction of ultrafine Cu_2O nanodomains, intricately coupled on the CeO_2 surface (Cu_2O/CeO_2), originating from the heterointerface comprised of ultrafine CuO nanodomains on the CeO_2 surface (CuO/CeO_2). When served as the electrocatalyst for the electrochemical CO_2 reduction reaction, Cu_2O/CeO_2 delivers a selectivity higher than 49 % towards CH_4 over a broad potential range from −1.2 V to

* Corresponding authors at: Department of Chemistry: Metalorganics and Inorganic Materials, Technische Universität Berlin, Straße des 17 Juni 135, Sekr. C2, 10623 Berlin, Germany (P.W. Menezes); and Institute of Functional Nano & Soft Materials (FUNSOM), Jiangsu Key Laboratory for Carbon-Based Functional Materials & Devices, Soochow University, 199 Ren'ai Road, Suzhou 215123, Jiangsu, China (Z. Kang).
E-mail addresses: hhuang0618@suda.edu.cn (H. Huang), yanlk924@nenu.edu.cn (L. Yan), prashanth.menezes@mailbox.tu-berlin.de, prashanth.menezes@helmholtz-berlin.de (P.W. Menezes), zhkang@suda.edu.cn (Z. Kang).

https://doi.org/10.1016/j.jcis.2024.05.212
Received 22 March 2024; Received in revised form 1 May 2024; Accepted 28 May 2024
Available online 29 May 2024

−1.7 V *vs*. RHE, maintaining negligible activity decay for 20 h. Notably, the highest selectivity for CH_4 reaches an impressive 70 % at −1.5 V *vs*. RHE. Through the combination of comprehensive analysis including synchrotron X-ray absorption spectroscopy, spherical aberration-corrected high-angle annular dark field scanning transmission electron microscope as well as the density functional theoretical calculation, the efficient production of CH_4 is attributed to the coherent interface between Cu_2O and CeO_2, which could converted from the original CuO and CeO_2 interface, ensuring abundant active sites and enhanced intrinsic activity and selectivity towards CH_4.

1. Introduction

The prospect of synthesizing chemical fuel through electrochemical CO_2 reduction reaction (CO_2RR) is highly promising, representing a robust pathway towards the realization of a carbon–neutral economy [1–4]. Through this electrochemical method, CO_2 is expected to undergo conversion into methane (CH_4), formic acid, carbon monoxide, methanol, ethylene, ethane, ethanol, and other hydrocarbons [5–18]. Since CH_4 is the fundamental component of natural gas and bears the highest energy density among hydrocarbon compounds, it stands as an appealing electrocatalytic reduction product of CO_2. However, the efficiency for the conversion from CO_2 to CH_4 is limited by the kinetically sluggish eight-electron transfer process [19]. In this regard, the development of electrocatalysts with high activity, selectivity, and stability is crucial for producing CH_4 through CO_2RR.

Copper (Cu) is one of the most effective electrocatalysts for CO_2RR [20–23]. However, it has relatively poor activity and selectivity in methanogenesis [2]. In contrast, the crystal plane of cuprous oxide (Cu_2O) offers controllability, and its structure is considerably stable, resulting in improved CH_4 production performance compared to pristine Cu [24]. In order to further enhance activity, researchers have integrated Cu_2O with various compounds (e.g., MOFs, CeO_2, graphene, SnO_x) [25–31]. This strategic combination exploits the synergistic interaction between Cu_2O and the introduced compound, triggering interfacial electron interaction and consequently enhancing the selectivity and activity for CO_2RR. For instance, Yi *et al.* [4] electrochemically reduced the surface Cu ion of CuHHTP to Cu_2O, uniformly distributing the formed Cu_2O on the remaining framework to create a highly active electrocatalyst, Cu_2O@CuHHTP. The reduction of the Cu center to Cu_2O released abundant uncoordinated hydroxyl groups near the active site, establishing hydrogen bonds with the intermediate and lowering the energy barrier for CH_4 formation. Yan et al. [31] modified CuO by CeO_2, where the interface effect of the catalyst reduced the energy of *CHO production. The rapid activation of water around CeO_2 accelerated the formation of *CHO, which promoted the C—C coupling step and improved the faradaic efficiency (FE) of C_{2+} products. Nevertheless, to the best of our knowledge, most of these reported composite systems still face challenges related to limited active area and structural stability, resulting in unsatisfactory efficiency for CH_4 production, especially across a wide potential range. Alternatively, CeO_2 can be used as a promising hybrid unit with Cu_2O because of its several merits including potential coherent interface, excellent chemical and composition stability, and modulated morphology. Despite these advantages, there remains a gap in research exploring the electrocatalytic CO_2RR through the combination of Cu_2O and CeO_2, which may offer potentially unlocking enhanced catalytic performance for CH_4.

On the other hand, recent studies have found that electrochemical reconstruction can enable the catalyst to exhibit excellent catalytic performance, especially for the oxygen evolution reaction (OER) [32–36]. This phenomenon is primarily attributed to the capacity of electrochemical reconstruction to induce the formation of a new active phase characterized by high dispersity and defective nanodomains [32–36]. For example, Jiang *et al.* [37] synthesized a new type of OER precatalyst ($Co_2(OH)_3Cl$), with distinctive physicochemical properties, facilitating phase reconstruction during OER through lattice anion etching. This reconstruction process continuously promoted OER activity. Zhu et al. [38] designed CuS nanomaterials with unique atomic arrangement sequences and certain cationic defects. After reconstruction, the formed has faster electron transport efficiency and a stronger Cu—S bond, which improves its OER performance. Interestingly, recent reports have indicated that Cu species with a lower chemical valence are formed from CuO during CO_2RR [39–43], implying the possible transformation from CuO to Cu_2O. However, owing to the large particle size, the phase reconstruction of CuO appears limited to the surface, resulting in an ambiguous identification of the real active structure, which deserves further attention. On the basis of this premise, one can envisage that employing ultrafine CuO particles with a size in the nanometer range in conjunction with CeO_2 to construct a (pre)catalyst could more readily trigger phase reconstruction, which could offer a chance to identify the real active structure. Unfortunately, there is still a lack of research on this pertinent investigation. Therefore, it is interesting to devise a strategy that allows to form an active intricately coupled Cu_2O/CeO_2 interface via the *in-situ* reconstruction of CuO/CeO_2 heterophase.

Motivated by the aforementioned considerations, the heterointerface consisting of ultrafine CuO nanodomains grown on the surface of CeO_2 (CuO/CeO_2) was initially constructed through hydrothermal treatment followed by calcination, during which a small amount of Cu ions was introduced during synthesis to prevent potential aggregation and agglomeration of CuO. Subsequently, CuO/CeO_2 was employed as the precatalyst for the electrocatalytic conversion of CO_2 to CH_4. Notably, the optimized electrocatalyst (Ce-Cu-10) exhibited outstanding selectivity towards CH_4 (>70 %), surpassing the performance of most Cu-based catalysts. Furthermore, in a wide potential range from −1.2 V to −1.7 V *vs*. RHE, it delivers a CH_4 selectivity higher than 49 % with a total current density of current density is $-23.4\ mA{\cdot}cm^{-2}$, showing excellent catalytic stability. Complementary X-ray absorption (XAS) and spherical aberration-corrected high-angle annular dark field scanning transmission electron microscope (SAC-HAADF-TEM) characterizations revealed a synergistic reconstruction from a coherent interface between ultrafine CuO and bulk CeO_2 to that between ultrafine Cu_2O and bulk CeO_2. Additionally, density functional theoretical (DFT) calculations elucidated the rate-determining step of CO_2 to CH_4, which deepens the understanding of the catalytic mechanism at the molecular level. Our work also illustrates that in this unique heterostructure, the presence of CeO_2 is conducive to the adsorption of both CO_2 and proton, which contributes to the electrocatalytic conversion from CO_2 to CH_4 on the active Cu center. The findings in this work not only introduce a novel approach for designing highly efficient catalysts for the electrocatalytic reduction of CO_2 to CH_4 but also advance the fundamental research on precatalysts for CO_2RR catalysis and beyond.

2. Experimental section

2.1. Materials

Cerium nitrate hexahydrate ($Ce(NO_3)_3{\cdot}6H_2O$, 99.5 %) was purchased from Macklin. Nafion (~5 %) was purchased from UTEPO Technology Suzhou Co. Copper(ii) nitrate hydrate ($Cu(NO_3)_3{\cdot}3H_2O$, AR) was purchased from Sinopharm. Sodium hydroxide was purchased from Sodium hydroxide (NaOH, 98 %). Potassium bicarbonate ($KHCO_3$, 99.7 %) was purchased from Aladdin.

2.2. Synthesis of CeO_2, CuO, Ce-Cu-x (x = 6, 8, 10 and 12. X is the molar ratio of Ce/Cu)

A hydrothermal method was used to synthesize CeO_2. Typically, 0.744 g of $Ce(NO_3)_3{\cdot}6H_2O$ and 9.6 g of NaOH were mixed and dissolved in 40 mL of deionized (DI) water. The mixed solution was ultrasonicated for an additional 30 min at room temperature and then the inks were transferred into a 100 mL Teflon reactor. The Teflon reactor was tightly sealed and subjected to hydrothermal treatment in an oven at 350 K for 24 h. After cooling down, the white precipitate obtained was collected, washed with ultrapure water and ethanol three times, and dried overnight in a vacuum oven at 80 °C. The yellow powder obtained after drying was calcined in a muffle furnace at 450 °C for 3 h to get CeO_2.

The CeO_2 was then used to prepare Ce-Cu-x. In order to prepare Ce-Cu-8, Ce-Cu-10 and Ce-Cu-12, 0.1 g CeO_2 was ultrasonically dispersed in 20 mL deionized water, and then 17.6 mg, 14.1 mg and 11.7 mg Cu $(NO_3)_3{\cdot}3H_2O$ were added, respectively. After stirring for 20 min, 0.5 mol/L Na_2CO_3 was added to adjust the pH to 9–10 of the solution. The mixed solution was centrifuged at 8000 rpm for five minutes, then it was dried overnight. The obtained powder was calcined in a muffle furnace at 500 °C for 3 h. The preparation process of CuO was the same as that of Ce-Cu-8 except that CeO_2 was not added.

3. Results and discussion

To validate our concept, we prepared a sample with the Ce to Cu molar ratio of 10:1 (hereafter referred to as Ce-Cu-10), along with samples having Ce to Cu molar ratios of 1:0, 8:1, 12:1, and 0:1 for comparison (defined as CeO_2, Ce-Cu-8, Ce-Cu-12, and CuO, respectively, and the distribution of element content in each sample is shown in Table S1). X-ray diffraction (XRD) was employed to characterize the structure of the prepared samples. As illustrated in Fig. 1a, the diffraction peak positions in the XRD patterns of CeO_2 and Ce-Cu-10 closely matched those of standard CeO_2 (PDF#81-0792). Fig. 1b represents a local enlargement of the XRD patterns depicted in Fig. 1a. It is evident that the positions of the diffraction peaks in the XRD patterns of CeO_2 and Ce-Cu-10 are essentially consistent, implying the copper species tend to exist in the form of copper oxide rather than as Cu-doped CeO_2. To further exclude the influence of potential test factor on the diffraction peak positions, the commercial pure Fe powder was used as an internal standard, which was mixed with the prepared powder samples (50 wt %), and their XRD patterns were measured under the same conditions

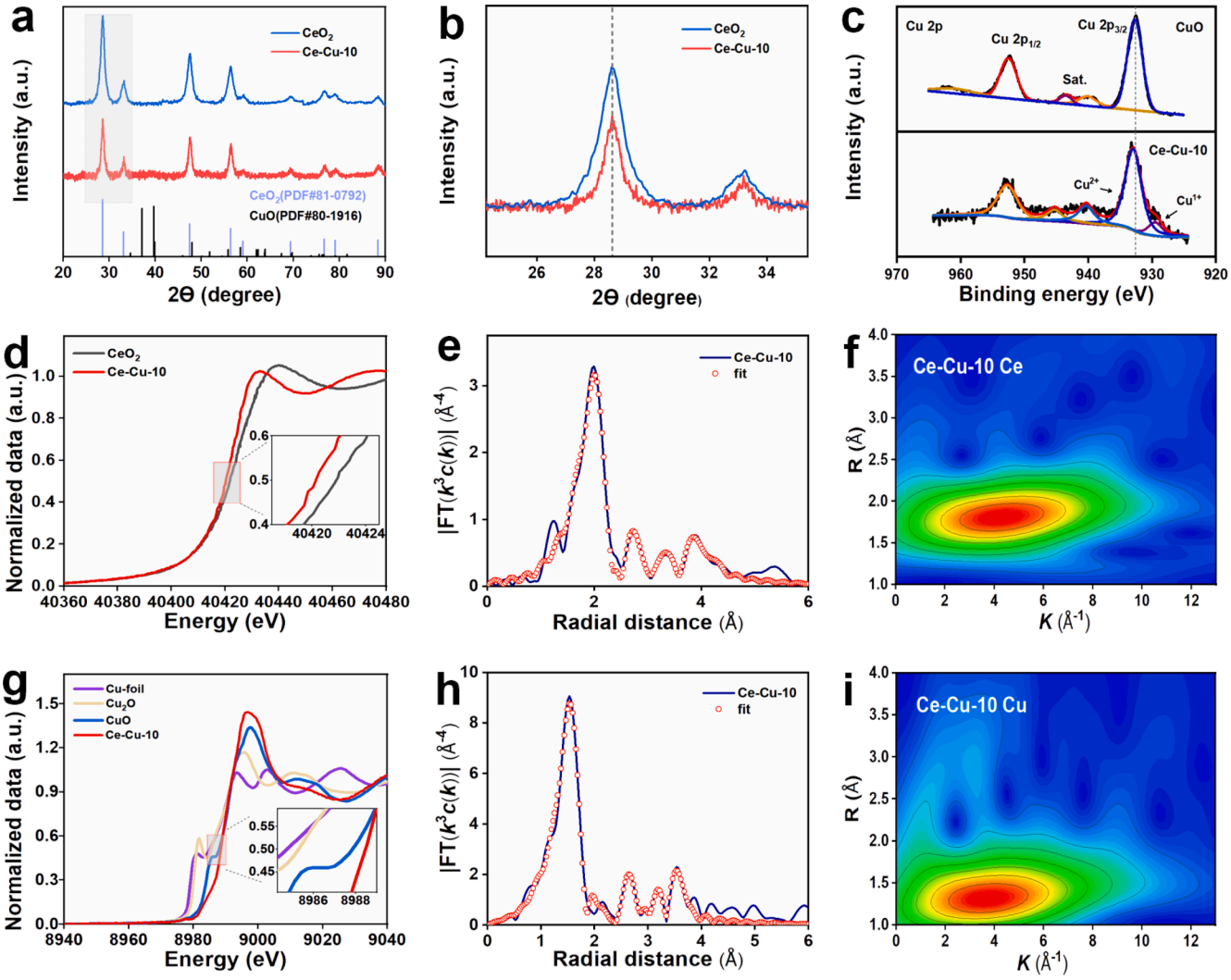

Fig. 1. (a) XRD patterns of the as-prepared CeO_2 and Ce-Cu-10 as well as (b) the associated magnified region in the two theta range from 25 to 35 degrees. (c) High resolution XPS spectra of Cu 2p in CuO and Ce-Cu-10. (d) Normalized XANES and the enlarged white line (the inset) spectra of Ce *K*-edge in Ce-Cu-10 and the standard sample CeO_2. (e) EXAFS pattern for the Ce *K*-edge in CeO-Cu-10 fitted in R space. (f) Wavelet transformation pattern of Ce *K*-edge of Ce-Cu-10. (g) Normalized XANES and the enlarged white line (the inset) spectra of Cu *K*-edge in Ce-Cu-10, CuO, Cu_2O and Cu-foil. (h) EXAFS pattern for the Cu *K*-edge in CeO-Cu-10 fitted in R space. (i) Wavelet transformation pattern of Cu *K*-edge of Ce-Cu-10.

(Fig. S1b). The results demonstrated that, compared with CeO_2, there is no shift for the characteristic peaks in the XRD patterns of as-prepared Ce-Cu-8, Ce-Cu-10, and Ce-Cu-12. This implies that Cu species were not doped into the Ce sites of the CeO_2 lattice.

X-ray photoelectron spectroscopy (XPS) experiments were further carried out to decouple the surface chemical state of Cu species. The high resolution XPS spectra of Cu 2p in Ce-Cu-10 and CuO are displayed and compared in Fig. 1c. It could be seen that the peak for Cu 2p (932.98 eV) in Ce-Cu-10 shifted to a higher energy than that (932.78 eV) in CuO. The peak at Cu $2p_{3/2}$ (929.58 eV) of Ce-Cu-10 was assigned to Cu^+, primarily resulting from oxygen vacancies in CeO_2 [43–46]. The XPS spectra of Ce 3d in CeO_2 (Fig. S2a) were deconvoluted into eight peaks, corresponding to the Ce $3d_{5/2}$ (v, 882.28 eV; ν″, 885.28 eV; ν″, 888.88 eV; ν‴, 898.16 eV) and Ce $3d_{3/2}$ states (u, 900.78 eV; u′, 902.98 eV; u″, 907.48 eV; u‴, 916.48 eV). The ν, ν′, u, and u‴ peaks were assigned to Ce^{3+} species, while the remaining four peaks were assigned to Ce^{4+} species. Compared with Ce 3d of CeO_2, Ce-Cu-10 shifted to the lower energy. The above observations strongly indicated that electrons were transferred from Cu species to the surface of CeO_2, being consistent with the results of XPS spectra for Cu 2p.

On the other hand, synchrotron radiation X-ray absorption near-edge structure (XANES) and extended X-ray absorption fine structure (EXAFS) analyses were to gain deeper insights into the chemical states and coordination environments of Ce and Cu in Ce-Cu-10 at the atomic scale (Fig. 1d–i, Figs. S3–S5). In comparison with the XANES spectra for the Ce *K*-edge of CeO_2 (Fig. 1d), Ce-Cu-10 exhibited a blue shift, signifying a slight reduction in the valence state of Ce in Ce-Cu-10. This finding was consistent with the XPS results of Ce 3d in Ce-Cu-10. Furthermore, the coordination of Ce and Cu in K and R spaces was clearly delineated using wavelet transform-EXAFS (WT-EXAFS). The Ce K-edge and Cu K-edge WT-EXAFS patterns of Ce-Cu-10 are shown in Fig. 1f and 1i, respectively. Similar to the EXAFS spectrum (Fig. 1e, h), significant WT signals related to Ce—O, Ce—Cu, and Ce—Ce bonds could be observed, while WT signals of Cu—O, Cu—Cu, and Cu—Ce were detected for Cu element. Fig. 1g displayed the XANES spectra for the Cu K-edge of Ce-Cu-10, along with those for Cu foil, commercial CuO, and commercial Cu_2O as reference. Fig. 1g shows the XANES spectra of the Cu K-edge. The energy position of the pre-edge of Ce-Cu-10 is very close to the energy position of commercial CuO, indicating that the oxidation state of Cu in Ce-Cu-10 is close to +2. Fig. S4b illustrates the Fourier transform EXAFS spectra of Ce-Cu-10 and the references (Cu foil, commercial CuO, and Cu_2O). It could be concluded that the EXAFS spectrum of Ce-Cu-10 was similar to that of CuO reference. In addition, the k3χ (k) oscillation curve of Ce-Cu-10 at the Cu K-edge

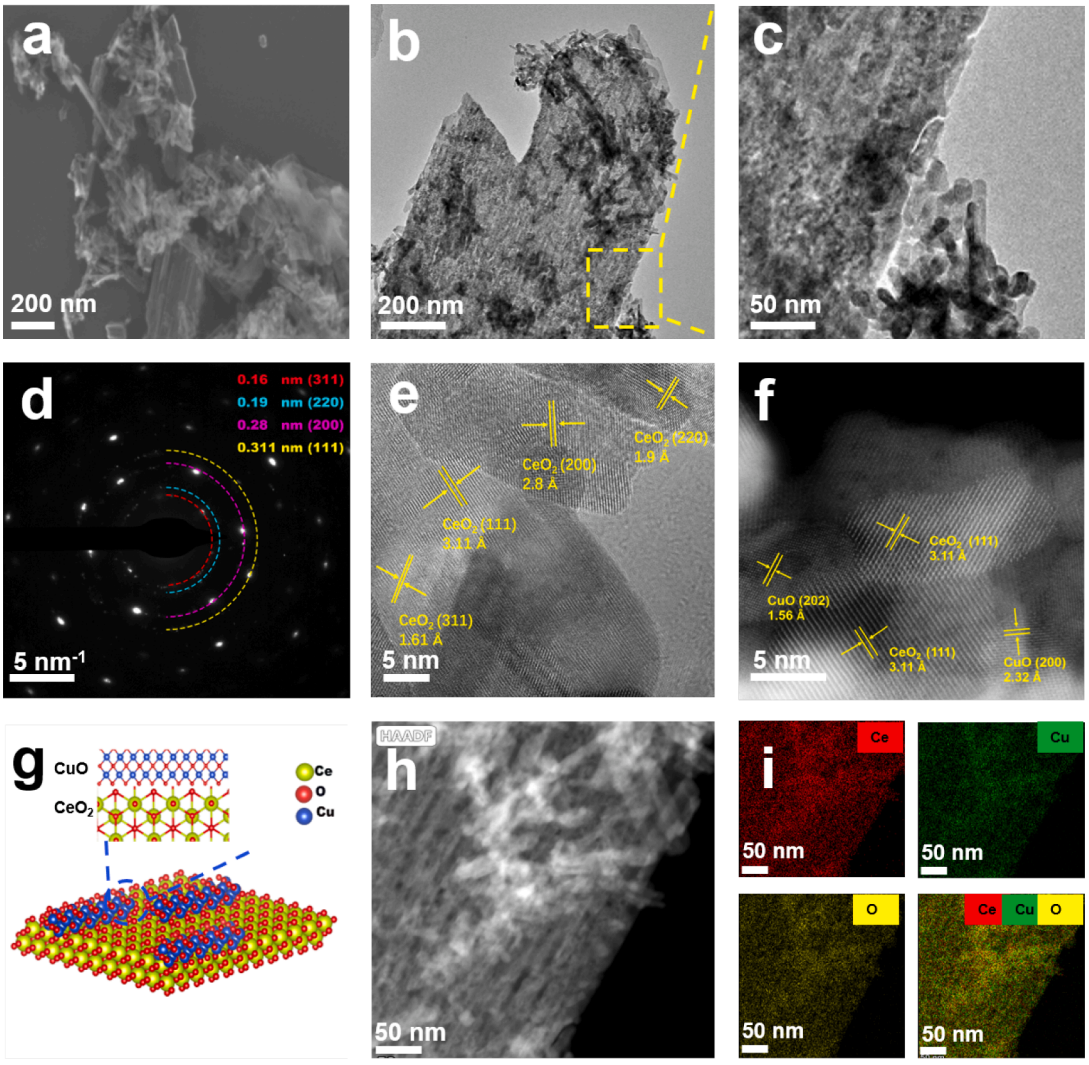

Fig. 2. Morphological and structural characterization of Ce-Cu-10. (a) FESEM, (b) TEM, (c) magnified TEM, (d) corresponding SAED, (e) HRTEM, (f) and SAC-HAADF-STEM images. (g) Surface structure diagram of Ce-Cu-10 (The blue, yellow, and red atoms represent Cu, Ce, and O atoms, respectively). (h) HAADF-STEM pattern of Ce-Cu-10 and its corresponding EDS mapping images of (i) Ce, Cu, and O. (For interpretation of the references to colour in this figure legend, the reader is referred to the web version of this article.)

exhibited a similar trend to that of commercial CuO powder in shape and oscillation frequency, indicating that the Cu species in Ce-Cu-10 bore similar properties to those of CuO (Fig. S4a). These results collectively suggested that Cu in Ce-Cu-10 should be present in the form of CuO which had a strong charge coupling with CeO_2, which could be supported by the formation of minor Ce—Cu bond observed in the EXAFS patterns for Cu K-edge and Ce K-edge in Ce-Cu-10.

The morphology of the as-prepared five samples was further examined by field-emission scanning electron microscopy (FESEM). The pristine CuO compound exhibited a granular shape with an average particle size of about 100 nm (Fig. S6a). In contrast, the pristine CeO_2 displayed a pseudo-nanorod morphology (Fig. S6b). Upon the introduction of Cu species, the morphology was largely retained, closely resembling that of CeO_2 (Fig. 2a, Fig. S6c, d). The microstructure of Ce-Cu-10 was further characterized by transmission electron microscopy (TEM). Consistent with the FESEM images, TEM revealed a pseudo-nanorod morphology (Fig. 2b, c). The corresponding selected area electron diffraction pattern (SAED) showed four diffraction rings that could be indexed to the (111), (200), (220), and (311) facets of the CeO_2 phase, respectively (Fig. 2d). The high-resolution TEM images (HRTEM) shown in Fig. 2e depicted lattice distances of 0.311, 0.28, 0.19, and 0.16 nm, corresponding to the (111), (200), (220), and (311) facets of CeO_2 phase, respectively [42,47]. Intriguingly, no lattice fringes belonging to CuO were observed by HRTEM. To further clarify the existence or presence of CuO in the form of ultrafine size, spherical aberration-corrected high-angle annular dark field scanning transmission electron microscope (SAC-HAADF-TEM) (Fig. 2f). As expected, in addition to the (111) facet of CeO_2 (0.311 nm), 0.156 and 0.172 nm of lattice distances corresponding to (202) and (200) facets of CuO were also identified. The quantum size of CuO could be a reason why it was challenging to identify its presence by XRD and HRTEM. Fig. 2g schematically displayed the coupling between the CeO_2 matrix and ultrafine CuO nanodots, where the former not only tuned the structure of the latter but also physically confined it. In addition, the high-angle annular dark field scanning transmission electron microscope (HAADF-STEM) and corresponding EDS elemental mapping images for the representative Ce-Cu-10 verified the uniform distribution of Ce, O, and Cu elements in the Ce-Cu-10 composite, confirming that Cu species were uniformly loaded on CeO_2 (Fig. 2h, i).

The electrochemical performance of Ce-Cu-10 for the CO_2 reduction reaction (CO_2RR) was evaluated in a sealed H-cell with a CO_2-saturated 0.5 M $KHCO_3$ *via* the constant potential method over a potential range from −1.2 to −1.7 V *vs.* RHE. Gas chromatography (GC) was employed for the detection and quantification of gaseous products, while liquid products were analyzed using a nuclear magnetic resonance spectrometer (NMR) after completion of the electrochemical reaction. For a comprehensive comparison, the CO_2RR activity of CeO_2, synthetic CuO, and other control samples was also examined under identical test conditions. Fig. 3a–c show the CO_2RR products containing both gas and liquid phases, with the gas phases being the predominant products. The FE of the gas products for Ce-Cu-10, CeO_2, and CuO is displayed in Fig. 3a–c. In the case of Ce-Cu-10, even at an initial cathode potential of −1.2 V, CH_4 was observed (49.03 %), accompanied by a certain amount of H_2 gas (Fig. 3b). With an increase in cathode potential, the FE yield of CH_4 further increased, while the yield of H_2 decreased. At −1.5 V (*vs.* RHE), the FE for CH_4 formation on Ce-Cu-10 reached 70.1 % with almost no other C_{1+} products. However, the FE of CH_4 for CeO_2 and CuO was almost zero and 8.44 % at the same potential, respectively (Fig. 3a and 3c). Compared with Cu_2O, Ce-Cu-8 and Ce-Cu-12 (Figs. S7–S9), Ce-Cu-10 has the highest CH_4 selectivity at −1.5 V *vs.* RHE. Actually, except for the gas products, some liquid products by CO_2RR were also identified. The liquid phase products of the samples in the electrocatalytic CO_2RR were checked by NMR, which are shown in Fig. S8 and Fig. S9. Note that the total FEs for all the samples are close to 100 %, indicating that nearly all products were detected. Consequently, when compared with previously reported Cu and Ce-based catalysts for CO_2RR, Ce-Cu-10 demonstrated a significantly higher CH_4 production (Fig. 3d, Table S2). To further demonstrate the superior catalytic activity of Ce-Cu-10, the

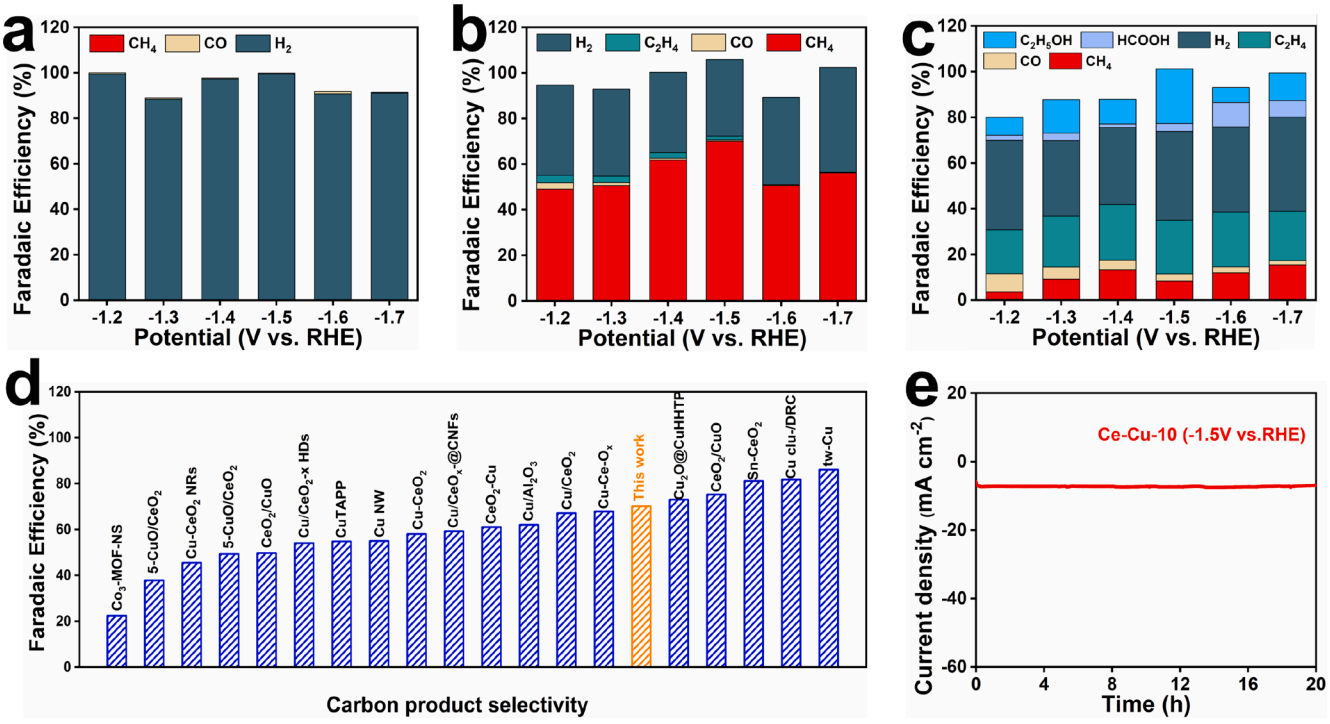

Fig. 3. Electrocatalytic CO_2RR of CeO_2, Ce-Cu-10, and CuO. Product distributions and corresponding faradaic efficiencies produced by (a) CeO_2 (b) Ce-Cu-10 and (c) CuO at different applied potentials in CO_2-saturated 0.5 M $KHCO_3$ electrolyte. (d) Comparison of the ethylene faradaic efficiency of Ce-Cu-10 with previously reported state-of-the-art Cu-based catalysts (the details are provided in Table S2). (e) Stability test of Ce-Cu-10 at −1.5 V (*vs.* RHE) in CO_2-saturated 0.5 M $KHCO_3$ electrolyte.

linear sweep voltammetry (LSV) curves towards CO_2RR in N_2-saturated and CO_2-saturated 0.5 M $KHCO_3$ solution (Fig. S10a and 10b) were measured. It is well known that the electrode material mainly competes for HER in the N_2-saturated solution, while CO_2RR is more favorable in the CO_2-saturated solution. Compared with the CeO_2 catalyst, the Ce-Cu-10 catalyst exhibited a larger positive current difference in the CO_2-saturated electrolyte, indicating that it had higher catalytic activity for CO_2RR. Specifically, Ce-Cu-10 had a higher current density (−23.43 $mA{\cdot}cm^{-2}$) than CeO_2 (−1.97 $mA{\cdot}cm^{-2}$) at −1.5 V *vs*. RHE, highlighting that the introduction of ultrafine CuO significantly enhanced the catalytic activity of CO_2RR (Fig. S10a).

To probe the reasons for the high activity, the electrochemical surface area (ECSA) in the potential range of 0.75–0.85 V *vs*. RHE in CO_2-saturated 0.5 M $KHCO_3$ was evaluated for the electrocatalysts (Fig. S11a–e). ECSA was evaluated by measuring the electric double layer (C_{dl}) value. As shown in Fig. S11f, the C_{dl} (0.17 $mF{\cdot}cm^{-2}$) of the Ce-Cu-10 catalyst was larger than those of other reference catalysts, suggesting an abundance of potential active sites, thereby enhancing catalytic current density.

The electrochemical impedance spectroscopy (EIS, Fig. S10c) revealed that in the CO_2RR process, Ce-Cu-10 exhibited the smallest charge transfer resistance (R_{ct}). A smaller R_{ct} signifies faster electron transfer from the catalyst to CO_2, a pivotal factor in enhancing catalytic performance. Furthermore, we measured CO_2 adsorption isotherms of Ce-Cu-8, Ce-Cu-10, Ce-Cu-12, CeO_2, and CuO at 25 °C (Fig. S12) and found that the CO_2 adsorption capacity by CuO is the lowest (95.83 $\mu mol{\cdot}g^{-1}$). Remarkably, the adsorption capacity of CO_2 by Ce-Cu-10 was increased by 126 % after loading it on CeO_2 (217.02 $\mu mol{\cdot}g^{-1}$). The Brunauer–Emmett–Teller (BET) surface areas of CeO_2, Ce-Cu-10, and CuO are 70.46 ± 0.11, 55.06 ± 0.03, and 8.95 ± 0.11 $m^2{\cdot}g^{-1}$, respectively (Table S3). These results confirmed enhanced CO_2 adsorption in the composite material, contributing to sufficient interaction of CO_2 with the catalyst surface, thereby mitigating the mass transfer limitation of CO_2RR at high reduction potential.

Since durability is a crucial metric for describing catalytic performance in CO_2RR, the electrochemical stability of the Ce-Cu-10 catalyst was assessed through long-term chronoamperometry at an optimal overpotential of −1.5 V *vs*. RHE. As depicted in Fig. 3e, the current density remained remarkably stable throughout a continuous 20-hour test, signifying the robust and stable CO_2RR activity of the Ce-Cu-10 catalyst. The post-stability of the catalyst was characterized by XRD, and the pattern was nearly identical to that of a pristine one (Fig. S13). The high resolution Cu 2p XPS spectra showed the intensified signal for Cu^+, suggesting the reduction of Cu species during CO_2RR, while the high resolution Cu 2p XPS spectra after CO_2RR tests cycling displayed characteristics similar to the fresh catalyst (Fig. S14). Further insights into the chemical states of Cu and Ce after CO_2RR were gained through XAS measurements on the Cu *K*-edge and Ce *K*-edge in Ce-Cu-10. Substantial changes were observed in the XANES and EXAFS spectra of the Ce-Cu-10 catalyst after the chronoamperometry test conducted under optimal performance conditions (Fig. 4, Figs. S3 and S4). The XANES pattern for Ce *K*-edge showed a slight negative shift as compared to that before CO_2RR, probably due to the local structural or interfacial variation (Fig. 4a). Corresponding EXAFS and WT patterns demonstrated subtle changes in the local structure (Fig. 4b and 4c). The XANES pattern for Cu *K*-edge in Ce-Cu-10 catalyst post reaction showed an apparent shift to the lower energy, confirming that the valence state of Cu decreased to close to +1 after the durability test (Fig. 4d). Additionally, EXAFS patterns and WT signals revealed the presence of Cu species in the form of Cu_2O (Fig. S4b, Fig. 4e, and 4f), strongly affirming the transformation of CuO to Cu_2O during CO_2RR. Besides, the preserved Ce—Cu bond suggested a strong coupling between CeO_2 and the formed Cu_2O.

The morphology of the Ce-Cu-10 catalyst after CO_2RR was then conducted through FESEM and TEM, which indicated that the morphology remained essentially unchanged compared to the pre-reaction state (Fig. 5a–c). The SAED and HRTEM images exhibited clear lattice spacings of 0.311, 0.28, and 0.19 nm, corresponding to (111), (200), and (220) facets of CeO_2, respectively, with no identification of Cu-based phases. However, SAC-HAADF-STEM images

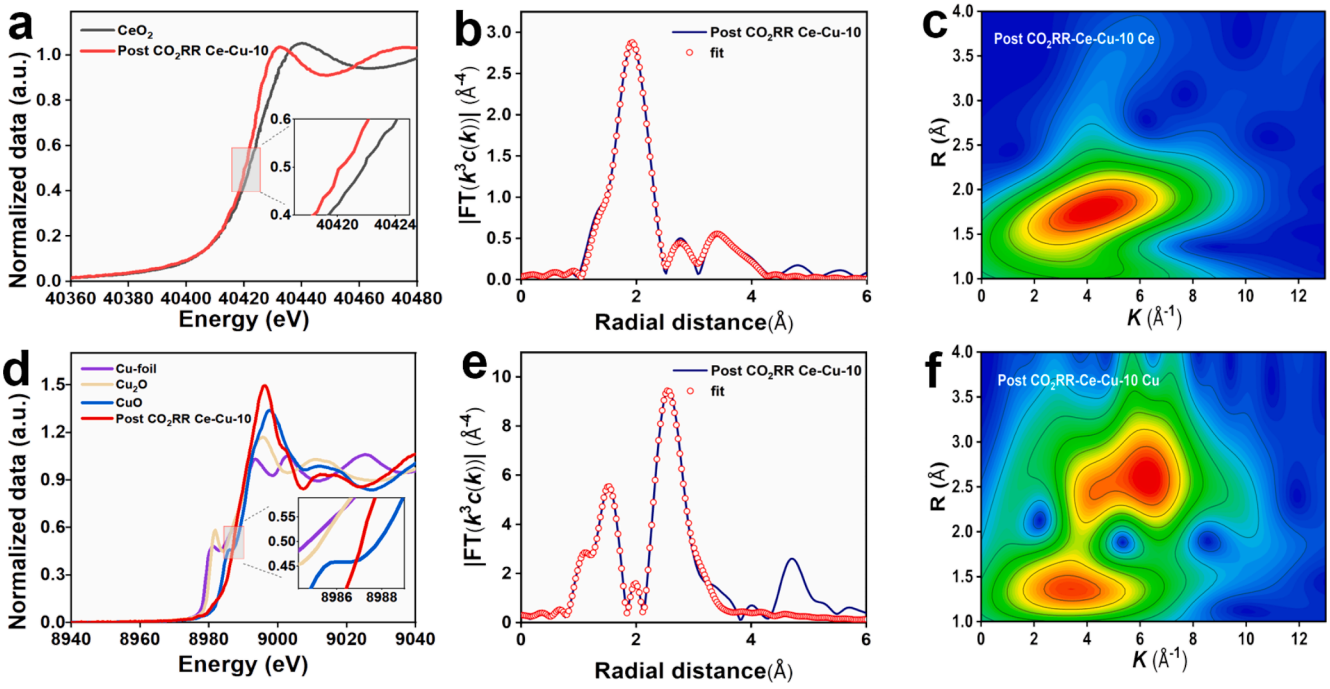

Fig. 4. (a) Normalized XANES and the enlarged white line (the inset) spectra of Ce *K*-edge in post CO_2RR Ce-Cu-10 and the standard sample CeO_2. (b) Post CO_2RR Ce-Cu-10 fitted in R space. (c) Wavelet transformation pattern of Ce *K*-edge EXAFS of post CO_2RR Ce-Cu-10. (d) Normalized XANES and the enlarged white line (the inset) spectra of Cu *K*-edge in post CO_2RR Ce-Cu-10, CuO, Cu_2O and Cu-foil. (e) Post CO_2RR CeO-Cu-10 fitted in R space. (f) Wavelet transformation pattern of Cu *K*-edge EXAFS of post CO_2RR Ce-Cu-10.

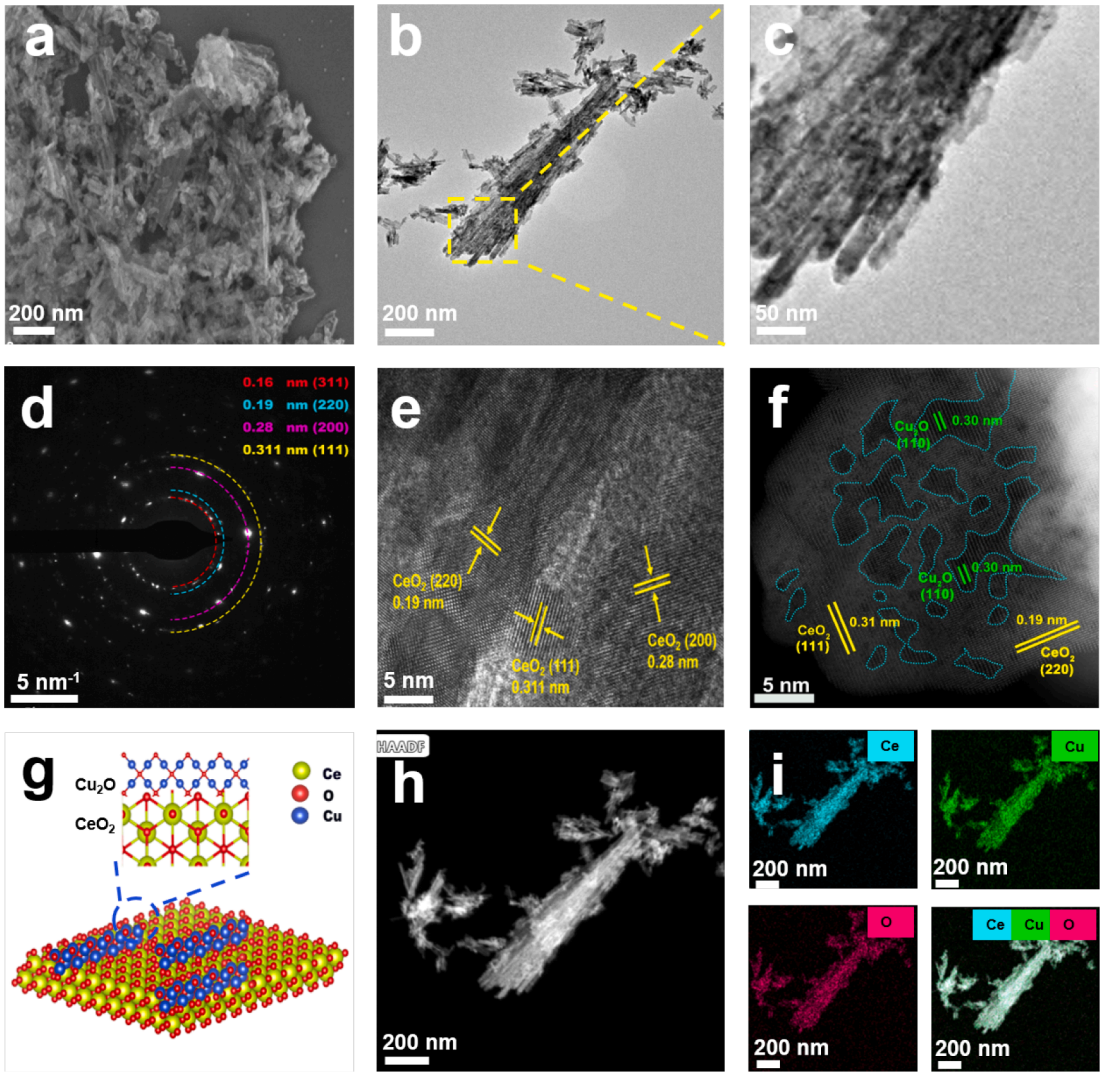

Fig. 5. Morphological and structural characterization of post CO_2RR Ce-Cu-10. (a) FESEM, (b) TEM, (c) magnified TEM, (d) corresponding SAED, (e) HRTEM, (f) and SAC-HAADF-STEM images. (g) Surface structure diagram of Ce-Cu-10 (The blue, yellow, and red atoms represent Cu, Ce, and O atoms, respectively). (h) HAADF-STEM pattern of Ce-Cu-10 and its corresponding EDS mapping images of (i) Ce, Cu, and O. (For interpretation of the references to colour in this figure legend, the reader is referred to the web version of this article.)

revealed discernible lattice fringes of 0.31 and 0.19 nm corresponding to (1 1 1) and (2 2 0) facets of CeO_2, as well as lattice fringes of 0.3 corresponding to (1 1 0) facet of Cu_2O [16], consistent with the XAS results. Further careful examination disclosed the uniform distribution of Cu_2O nanodomains onto CeO_2 in a possibly coherent growth manner, likely owing to the lattice confinement of CeO_2 toward Cu_2O (Fig. 5g). The STEM-HAADF and corresponding elemental mappings confirmed the even distribution of Ce, Cu, and O species on the surface of the pseudo-nanorod (Fig. 5h and 5i).

DFT calculations were carried out to gain in-depth insights into the electrocatalytic CO_2 reduction on the Cu_2O (1 1 0)-CeO_2 (1 1 1) surface. First of all, we constructed a structural model Cu_2O (1 1 0) cluster loaded onto the (1 1 1) surface of CeO_2 (Fig. 6a). Bader charge analysis revealed a positive charge of +0.53 e^- on CeO_2 (1 1 1). This observation implied that electrons were transferred from Cu_2O to CeO_2 at the Cu_2O/CeO_2 interface, favoring the progression of the CO_2RR. This electron transfer trend was further visualized through charge density differences (Fig. 6b). Subsequently, we calculated the adsorption free energy of intermediates at the Cu_2O/CeO_2 interface and explored the selective hydrogenation steps in the catalytic CO_2 reduction to hydrocarbon fuels (CH_4). As shown in Fig. 6c, the maximum Gibbs energies (ΔG_{max}) for converting CO_2 to CH_4 on the Cu_2O/CeO_2 was HCOO* → H_2COO* with a much higher free energy change of 0.65 eV, which was considered as the potential determining step (PDS).

Fig. S15 illustrates all the intermediate species involved in the process of CO_2 conversion to CH_4 for the two different reaction pathways analyzed in this study. Firstly, H was easily adsorbed on Cu at the Cu_2O/CeO_2 interface with a ΔG of 0.29 eV, and subsequently capturing a CO_2 molecule to form HCOO* intermediate ($\Delta G = -0.66$ eV). The formation of H_2COO* needed a ΔG of 0.65 eV. Following this, the H^+/e^- pair tends to adsorb onto the unreacted O atom of CO_2 to generate the H_2COOH* intermediate. H_2CO* was more likely to be obtained because of the aforementioned intermediate formation. The ΔG for the formation of CH_3O* was 0.27 eV. The hydrogenation of CH_3O* occurred on the C atom to form CH_4 + O* or on the O atom to form CH_3OH* with the ΔG of 0.73 eV and −1.08 eV, respectively. Forming CH_3OH* was more energetically favorable than CH_4 + O*. CH_3OH* hydrogenated into CH_3* with the ΔG of 0.42 eV. The final step in the hydrogenation process to form methane was an exothermic process of ($\Delta G = -0.92$ eV). Corresponding geometric structures of intermediates along the optimal reaction pathway on Cu_2O/CeO_2 are shown in Fig. 6d. In summary, the orange line in Fig. 6c delineates the most favorable pathway in our study, encompassing the intermediate species of H* → HCOO → H_2COO* → H_2COOH* → H_2CO* → H_3CO* → H_3COH* → CH_3* → CH_4.

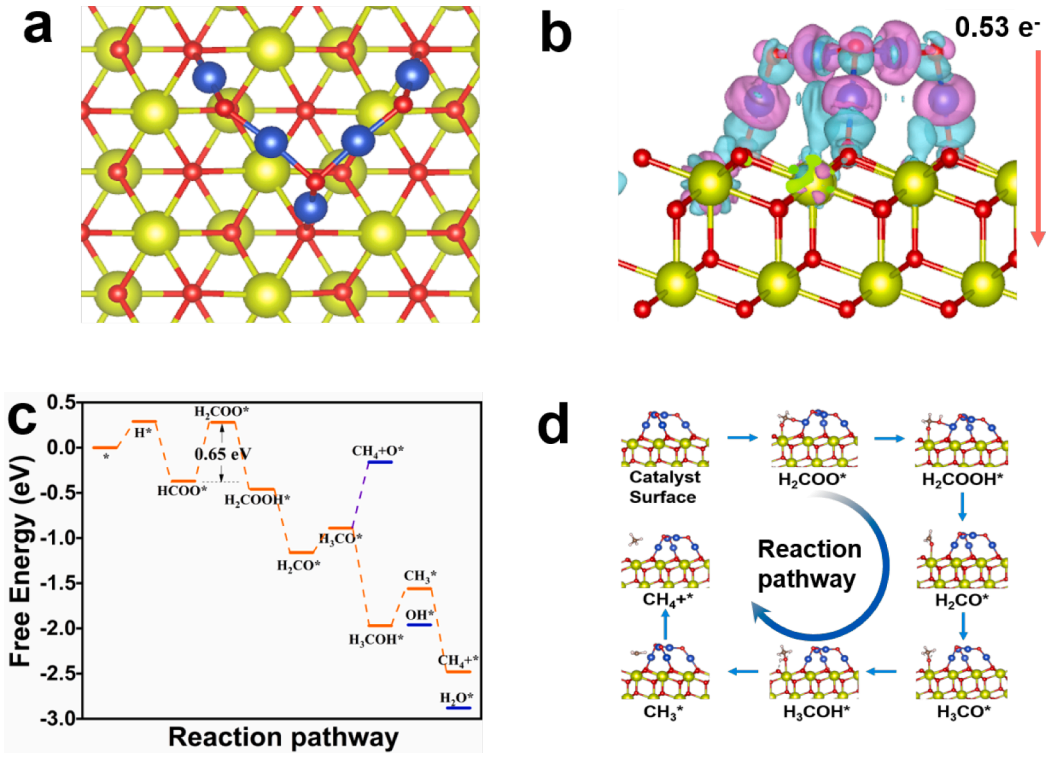

Fig. 6. (a) Top view of the slab model used for the computational study of the Cu_2O-CeO_2 (1 1 1) surface; (b) differential charge densities of the Cu_2O-CeO_2 (1 1 1) surface. The charge density represented in blue and purple shows the positive and negative phases, respectively. The isosurface was set to 0.006 e/Å^3. (c) The Gibbs free energy diagrams for the CO_2RR on (a) Cu_2O-CeO_2 at the applied potential. The blue, yellow, and red atoms are Cu, Ce, and O, respectively. The asterisk (*) represents a surface site for adsorption, and the maximum ΔG of the pathways is highlighted in orange. (d) The formation path of CH_4 on the catalyst surface was proposed. (For interpretation of the references to colour in this figure legend, the reader is referred to the web version of this article.)

This signifies that the Cu_2O/CeO_2 can effectively convert CO_2 to CH_4.

4. Conclusion

In summary, we introduced an ultralow amount of Cu species into the CeO_2 matrix to form a composite system comprising ultrafine CuO loaded on CeO for electrocatalytic CO_2 reduction to produce methane. A series of comprehensive investigations involving synchrotron radiation spectroscopy, spheric aberration-corrected TEM, and theoretical DFT calculations, unequivocally established that the composite system, featuring Cu_2O nanodomains loaded on the surface of CeO_2, undergoes reconstruction during CO_2RR, which not only exposed a large number of Cu^+ sites with high intrinsic catalytic activity, but also effectively promoted the structural stability by the coupling and confinement effect of CeO_2 unit towards Cu_2O. Consequently, this catalyst exhibited a notable high selectivity for CH_4 in a wide voltage range, and achieved a peak selectivity of 70.1 %, effectively suppressing the hydrogen evolution reaction. Moreover, when assembled as the electrode in H-cell configuration, its Faraday efficiency surpasses 70 % sustaining methane production over 20 h. This innovative approach, involving ultra-low loading of CuO on a CeO_2 support as a precatalyst, not only sheds light on the evolution mechanism of high-valence Cu in electrocatalysis but also provides novel insights and strategies for designing highly efficient electrocatalytic CO_2 reduction catalysts.

5. Experimental section

A detailed description of all applied methods can be found in the Supporting Information.

CRediT authorship contribution statement

Xiong Yan: Writing – original draft, Methodology, Data curation. **Shuo Wang:** Software, Data curation. **Ziliang Chen:** Validation, Conceptualization. **Yunjie Zhou:** Investigation, Data curation. **Hui Huang:** Writing – review & editing, Validation, Methodology. **Jie Wu:** Investigation. **Tiwei He:** Methodology. **Hongyuan Yang:** Data curation. **Likai Yan:** Writing – review & editing, Validation, Software. **Kaili Bao:** Methodology, Investigation. **Prashanth W. Menezes:** Writing – review & editing, Supervision, Conceptualization. **Zhenhui Kang:** Writing – review & editing, Validation, Supervision.

Declaration of competing interest

The authors declare that they have no known competing financial interests or personal relationships that could have appeared to influence the work reported in this paper.

Data availability

Data will be made available on request.

Acknowledgements

X. Yan and S. Wang contributed equally in this work. This work is supported by Natural Science Foundation of Jiangsu Province (BK20220028), National Key R&D Program of China (2020YFA0406104, 2020YFA0406101), National Natural Science Foundation of China (52272043, 52271223, 52202107, 52201269), Natural Science Foundation of Jiangsu Province (BK20210735, 21KJB430043), The Science and Technology Development Fund, Macau SAR (0009/2022/ITP), Collaborative Innovation Center of Suzhou Nano

Science & Technology, the 111 Project, and Suzhou Key Laboratory of Functional Nano & Soft Materials. P. W. Menezes greatly acknowledges support from the German Federal Ministry of Education and Research in the framework of the project Catlab (03EW0015A/B).

Appendix A. Supplementary material

Supplementary data to this article can be found online at https://doi.org/10.1016/j.jcis.2024.05.212.

References

[1] A.R. Woldu, Z. Huang, P. Zhao, L. Hu, D. Astruc, Electrochemical CO_2 reduction (CO_2RR) to multi-carbon products over copper-based catalysts, Coord. Chem. Rev. 454 (2022) 214340, https://doi.org/10.1016/j.ccr.2021.214340.

[2] S. Nitopi, E. Bertheussen, S.B. Scott, X. Liu, A.K. Engstfeld, S. Horch, B. Seger, I.E. L. Stephens, K. Chan, C. Hahn, J.K. Nørskov, T.F. Jaramillo, I. Chorkendorff, Progress and Perspectives of electrochemical CO_2 reduction on copper in aqueous electrolyte, Chem. Rev. 119 (2019) 7610–7672, https://doi.org/10.1021/acs.chemrev.8b00705.

[3] X. Duan, J. Xu, Z. Wei, J. Ma, S. Guo, S. Wang, H. Liu, S.X. Dou, Metal-free carbon materials for CO_2 electrochemical reduction, Adv. Mater. 29 (2017) 1701784, https://doi.org/10.1002/adma.201701784.

[4] W. Xi, P. Yang, M. Jiang, X. Wang, H. Zhou, J. Duan, M. Ratova, D. Wu, Electrochemical CO_2 reduction coupled with alternative oxidation reactions: electrocatalysts, electrolytes, and electrolyzers, Appl. Catal. B Environ. 341 (2024) 123291, https://doi.org/10.1016/j.apcatb.2023.123291.

[5] J. Yi, R. Xie, Z. Xie, G. Chai, T. Liu, R. Chen, Y. Huang, R. Cao, Highly selective CO_2 electroreduction to CH_4 by in situ generated Cu_2O single-type sites on conductive MOF: stabilizing key intermediates with hydrogen bond, Angew. Chem. Int. Ed. 59 (2020) 23641–23648, https://doi.org/10.1002/anie.202010601.

[6] Y.-Y. Liu, H.-L. Zhu, Z.-H. Zhao, N.-Y. Huang, P.-Q. Liao, X.-M. Chen, Insight into the effect of the d-orbital energy of copper ions in metal-organic frameworks on the selectivity of electroreduction of CO_2 to CH_4, ACS Catal. 12 (2022) 2749–2755, https://doi.org/10.1021/acscatal.1c04805.

[7] R. Zhao, P. Ding, P. Wei, L. Zhang, Q. Liu, Y. Luo, T. Li, S. Lu, X. Shi, S. Gao, A. M. Asiri, Z.M. Wang, X. Sun, Recent progress in electrocatalytic methanation of CO_2 at ambient conditions, Adv. Funct. Mater. 31 (2021) 2009449, https://doi.org/10.1002/adfm.202009449.

[8] F. Yang, A.O. Elnabawy, R. Schimmenti, P. Song, J. Wang, Z. Peng, S. Yao, R. Deng, S. Song, Y. Lin, M. Mavrikakis, W. Xu, Bismuthene for highly efficient carbon dioxide electroreduction reaction, Nat. Commun. 11 (2020) 1088, https://doi.org/10.1038/s41467-020-14914-9.

[9] G. Jia, M. Sun, Y. Wang, Y. Shi, L. Zhang, X. Cui, B. Huang, J.C. Yu, Asymmetric coupled dual-atom sites for selective photoreduction of carbon dioxide to acetic acid, Adv. Funct. Mater. 32 (2022) 2206817, https://doi.org/10.1002/adfm.202206817.

[10] J. Wang, Y. Huang, Y. Wang, H. Deng, Y. Shi, D. Wei, M. Li, C.L. Dong, H. Jin, S. S. Mao, S. Shen, Atomically dispersed metal–nitrogen–carbon catalysts with d-orbital electronic configuration-dependent selectivity for electrochemical CO_2-to-CO reduction, ACS Catal. 13 (2023) 2374–2385, https://doi.org/10.1021/acscatal.2c05249.

[11] S. Jin, Z. Hao, K. Zhang, Z. Yan, J. Chen, Advances and challenges for electrochemical reduction of CO_2 to CO: from fundamental to industrialization, Angew. Chem. Int. Ed. 60 (2021) 20627–20648, https://doi.org/10.1002/anie.202101818.

[12] R. Cao, D. Meng, M. Zhang, D. Si, M. Mao, Y. Hou, Y. Huang, Highly selective tandem electroreduction of CO_2 to ethylene over atomically isolated nickel-nitrogen site/copper nanoparticle catalysts, Angew. Chem. Int. Ed. 60 (2021) 25485–25492, https://doi.org/10.1002/anie.202111136.

[13] J. Billy, A.C. Co, Reducing the onset potential of CO_2 electroreduction on CuRu bimetallic particles, Appl. Catal. B Environ. 237 (2018) 911–918, https://doi.org/10.1016/j.apcatb.2018.06.072.

[14] K. Yu, H. Wang, W. Yu, S. Li, X. Zhang, Z. Bian, Resource utilization of carbon dioxide and nitrate to produce value-added organonitrogen compounds through an electrochemical approach, Appl. Catal. B Environ. 341 (2024) 123292, https://doi.org/10.1016/j.apcatb.2023.123292.

[15] J. Zhang, T. Fan, P. Huang, X. Lian, Y. Guo, Z. Chen, X. Yi, Electro-reconstruction-induced strain regulation and synergism of Ag-In-S toward highly efficient CO_2 electrolysis to formate, Adv. Funct. Mater. 32 (2022) 2113075, https://doi.org/10.1002/adfm.202113075.

[16] X. Ma, Y. Zhang, T. Fan, D. Wei, Z. Huang, Z. Zhang, Z. Zhang, Y. Dong, Q. Hong, Z. Chen, X. Yi, Facet dopant regulation of Cu_2O boosts electrocatalytic CO_2 reduction to formate, Adv. Funct. Mater. 33 (2023) 2213145, https://doi.org/10.1002/adfm.202213145.

[17] Z. Chen, T. Fan, Y.Q. Zhang, J. Xiao, M. Gao, N. Duan, J. Zhang, J. Li, Q. Liu, X. Yi, J.L. Luo, Wavy SnO_2 catalyzed simultaneous reinforcement of carbon dioxide adsorption and activation towards electrochemical conversion of CO_2 to HCOOH, Appl. Catal. B Environ. 261 (2020) 118243, https://doi.org/10.1016/j.apcatb.2019.118243.

[18] Z. Chen, M.R. Gao, N. Duan, J. Zhang, Y.Q. Zhang, T. Fan, J. Zhang, Y. Dong, J. Li, Q. Liu, X. Yi, J.L. Luo, Tuning adsorption strength of CO_2 and its intermediates on tin oxide-based electrocatalyst for efficient CO_2 reduction towards carbonaceous products, Appl. Catal. B Environ. 277 (2020) 119252, https://doi.org/10.1016/j.apcatb.2020.119252.

[19] S. Chen, W.-H. Li, W. Jiang, J. Yang, J. Zhu, L. Wang, H. Ou, Z. Zhuang, M. Chen, X. Sun, D. Wang, Y. Li, MOF encapsulating N-heterocyclic carbene-ligated copper single-atom site catalyst towards efficient methane electrosynthesis, Angew. Chem. Int. Ed. 61 (2021) e20211445, https://doi.org/10.1002/anie.202114450.

[20] Y. Hori, Electrochemical CO_2 reduction on metal electrodes, Mod. Aspects Electrochem. 42 (2008) 89–189, https://doi.org/10.1007/978-0-387-49489-0_3.

[21] J. Yu, J. Wang, Y. Ma, J. Zhou, Y. Wang, P. Lu, J. Yin, R. Ye, Z. Zhu, Z. Fan, Recent progresses in electrochemical carbon dioxide reduction on copper-based catalysts toward multicarbon products, Adv. Funct. Mater. 31 (2021) 2102151, https://doi.org/10.1002/adfm.202102151.

[22] W. Lai, Z. Ma, J. Zhang, Y. Yuan, Y. Qiao, H. Huang, Dynamic evolution of active sites in electrocatalytic CO_2 reduction reaction: fundamental understanding and recent progress, Adv. Funct. Mater. 32 (2022) 2111193, https://doi.org/10.1002/adfm.202111193.

[23] X.-Q. Li, G.-Y. Duan, J.-W. Chen, L.-J. Han, S.-J. Zhang, B.-H. Xu, Regulating electrochemical CO_2RR selectivity at industrial current densities by structuring copper@poly(ionic liquid) interface, Appl. Catal. B Environ. 297 (2021) 120471, https://doi.org/10.1016/j.apcatb.2021.120471.

[24] R.M. Arán-Ais, R. Rizo, P. Grosse, G. Algara-Siller, K. Dembélé, M. Plodinec, T. Lunkenbein, S.W. Chee, B.R. Cuenya, Imaging electrochemically synthesized Cu_2O cubes and their morphological evolution under conditions relevant to CO_2 electroreduction, Nat. Commun. 11 (2020) 3489, https://doi.org/10.1038/s41467-020-17220-6.

[25] X. Yang, J. Cheng, X. Yang, Y. Xu, W. Sun, J. Zhou, Facet-tunable coral-like Mo_2C catalyst for electrocatalytic hydrogen evolution reaction, Chem. Eng. J. 451 (2023) 138977, https://doi.org/10.1016/j.cej.2022.138977.

[26] Y. Wang, H. Lei, S. Lu, Z. Yang, B. Bin Xu, L. Xing, T.X. Liu, Cu_2O nano-flowers/graphene enabled scaffolding structure catalyst layer for enhanced CO_2 electrochemical reduction, Appl. Catal. B Environ. 305 (2021) 121022, https://doi.org/10.1016/j.apcatb.2021.121022.

[27] Y. Zhang, D. Pan, Y. Tao, H. Shang, D. Zhang, G. Li, H. Li, Photoelectrocatalytic reduction of CO_2 to syngas via SnO_x-enhanced Cu_2O nanowires photocathodes, Adv. Funct. Mater. 32 (2021) 2109600, https://doi.org/10.1002/adfm.202109600.

[28] A. Alarcón, T. Andreu, C. Ponce de León, CeO_2-promoted Cu_2O-based catalyst sprayed on the gas diffusion layer for the electroreduction of carbon dioxide to ethylene, Mater. Adv. 5 (2024) 2377–2387, https://doi.org/10.1039/d3ma01009k.

[29] S. Ali, H. Ali, S.H. Bakhtiar, S. Ali, M. Zahid, A. Ismail, P.M. Ismail, A. Zada, I. Khan, H. Shen, R. Ullah, H. Khan, M. Bououdina, X. Wu, F. Raziq, L. Qiao, Bifunctional phosphate-modulated Cu_2O/CeO_2 redox heterojunction: a promising approach for proficient CO_2 reduction, J. Alloys Compd. 972 (2024) 172766, https://doi.org/10.1016/j.jallcom.2023.172766.

[30] Y. Pu, Y. Luo, X. Wei, J. Sun, L. Li, W. Zou, L. Dong, Synergistic effects of Cu_2O-decorated CeO_2 on photocatalytic CO_2 reduction: surface Lewis acid/base and oxygen defect, Appl. Catal. B Environ. 254 (2019) 580–586, https://doi.org/10.1016/j.apcatb.2019.04.093.

[31] X. Yan, C. Chen, Y. Wu, S. Liu, Y. Chen, R. Feng, J. Zhang, B. Han, Efficient electroreduction of CO_2 to C_{2+} products on CeO_2modified CuO, Chem. Sci. 12 (2021) 6638–6645, https://doi.org/10.1039/d1sc01117k.

[32] B.M. Hunter, H.B. Gray, A.M. Muller, Correction to Earth-abundant heterogeneous water oxidation catalysts, Chem. Rev. 116 (2016) 14919, https://doi.org/10.1021/acs.chemrev.6b00788.

[33] G. Wu, A.V. Santandreu, W. Kellogg, S. Gupta, O. Ogoke, H. Zhang, H. Wang, L. Dai, Carbon nanocomposite catalysts for oxygen reduction and evolution reactions: from nitrogen doping to transition-metal addition, Nano Energy 29 (2016) 83–110, https://doi.org/10.1016/j.nanoen.2015.12.032.

[34] L. Gao, X. Cui, C.D. Sewell, J. Li, Z. Lin, Recent advances in activating surface reconstruction for the high-efficiency oxygen evolution reaction, Chem. Soc. Rev. 50 (2021) 8428–8469, https://doi.org/10.1039/D0CS00962H.

[35] F.-Y. Chen, Z.-Y. Wu, Z. Adler, H. Wang, Stability challenges of electrocatalytic oxygen evolution reaction: From mechanistic understanding to reactor design, Joule 5 (2021) 1704–1731, https://doi.org/10.1016/j.joule.2021.05.005.

[36] G. Gao, Z. Sun, X. Chen, G. Zhu, B. Sun, Y. Yamauchi, S. Liu, Recent advances in Ru/Ir-based electrocatalysts for acidic oxygen evolution reaction, Appl. Catal. B Environ. 343 (2024) 123584, https://doi.org/10.1016/j.apcatb.2023.123584.

[37] H. Jiang, Q. He, X.-Y. Li, X. Su, Y. Zhang, S. Chen, S. Zhang, G. Zhang, J. Jiang, Y. Luo, P.M. Ajayan, L. Song, Tracking structural self-reconstruction and identifying true active sites toward cobalt oxychloride precatalyst of oxygen evolution reaction, Adv. Mater. 31 (2019) 1805127, https://doi.org/10.1002/adma.201805127.

[38] J. Zhu, S.T. Zi, N. Zhang, Y. Hu, L. An, P. Xi, Surface reconstruction of covellite CuS nanocrystals for enhanced OER catalytic performance in alkaline solution, Small 19 (2023) e2301762, https://doi.org/10.1002/smll.202301762.

[39] R. Yang, J. Duan, P. Dong, Q. Wen, M.-J. Wu, Y. Liu, Y. Liu, H. Li, T. Zhai, In situ halogen-ion leaching regulates multiple sites on tandem catalysts for efficient CO_2 electroreduction to C_{2+} products, Angew. Chem. Int. Ed. 61 (2022) e202116706, https://doi.org/10.1002/anie.202116706.

[40] X. Wang, K. Klingan, M. Klingenhof, T. Möller, J.F. de Araújo, I. Martens, A. Bagger, S. Jiang, J. Rossmeisl, H. Dau, P. Strasser, Morphology and mechanism of highly selective Cu(II) oxide nanosheet catalysts for carbon dioxide electroreduction, Nat. Commun. 12 (2021) 794, https://doi.org/10.1038/s41467-021-20961-7.

[41] J. Zhang, Y. Wang, Z. Li, S. Xia, R. Cai, L. Ma, T. Zhang, J.C. Ackley, S. Yang, Y. Wu, J. Wu, Grain boundary-derived Cu_+/Cu_0 interfaces in CuO nanosheets for low overpotential carbon dioxide electroreduction to ethylene, Adv. Sci. 9 (2022) 2200454, https://doi.org/10.1002/advs.202200454.
[42] M.V. Grabchenko, G.V. Mamontov, V.I. Zaikovskii, V. La Parola, L.F. Liotta, O. V. Vodyankina, The role of metal–support interaction in Ag/CeO_2 catalysts for CO and soot oxidation, Appl. Catal. B Environ. 260 (2020) 118148, https://doi.org/10.1038/s41467-020-17220-6.
[43] L. Xue, C. Zhang, J. Wu, Q. Fan, Y. Liu, Y. Wu, J. Li, H. Zhang, F. Liu, S. Zeng, Unveiling the reaction pathway on Cu/CeO_2 catalyst for electrocatalytic CO_2 reduction to CH_4, Appl. Catal. B Environ. 304 (2021) 120951, https://doi.org/10.1016/j.apcatb.2021.120951.
[44] Y. Wang, Z. Chen, P. Han, Y. Du, Z. Gu, X. Xu, G. Zheng, Single-atomic Cu with multiple oxygen vacancies on ceria for electrocatalytic CO_2 reduction to CH_4, ACS Catal. 8 (2018) 7113–7119, https://doi.org/10.1021/acscatal.8b01014.
[45] X. Wei, H. Cai, B. Nie, P. Guan, Y.-S. Cheng, X.-D. Xu, F. Wu, G. Yuan, Tuning interactions between CuO and CeO_2 for rationally controlling electroreduction of CO_2 to methane or ethylene, ACS Appl. Nano Mater. 5 (2022) 7259–7267, https://doi.org/10.1021/acsanm.2c01164.
[46] X. Yan, C. Chen, Y. Wu, S. Liu, Y. Chen, R. Feng, J. Zhang, B. Han, Efficient electroreduction of CO_2 to C_{2+} products on CeO_2 modified CuO, Chem. Sci. 12 (2021) 6638, https://doi.org/10.1039/D1SC01117K.
[47] Z. Ma, L. Sheng, X. Wang, W. Yuan, S. Chen, W. Xue, G. Han, Z. Zhang, H. Yang, Y. Lu, Y. Wang, Oxide catalysts with ultrastrong resistance to SO_2 deactivation for removing nitric oxide at low temperature, Adv. Mater. 31 (2019) 1903719, https://doi.org/10.1002/adma.201903719.